ADVANCED MATERIALS
www.advmat.de

Liquid-Templating Aerogels

Seyyed Alireza Hashemi, Ahmadreza Ghaffarkhah, Milad Goodarzi, Amir Nazemi, Gabriel Banvillet, Abbas S. Milani, Masoud Soroush, Orlando J. Rojas, Seeram Ramakrishna, Stefan Wuttke, Thomas P. Russell,* Milad Kamkar,* and Mohammad Arjmand**

Modern materials science has witnessed the era of advanced fabrication methods to engineer functionality from the nano- to macroscales. Versatile fabrication and additive manufacturing methods are developed, but the ability to design a material for a given application is still limited. Here, a novel strategy that enables target-oriented manufacturing of ultra-lightweight aerogels with on-demand characteristics is introduced. The process relies on controllable liquid templating through interfacial complexation to generate tunable, stimuli-responsive 3D-structured (multiphase) filamentous liquid templates. The methodology involves nanoscale chemistry and microscale assembly of nanoparticles (NPs) at liquid–liquid interfaces to produce hierarchical macroscopic aerogels featuring multiscale porosity, ultralow density (3.05–3.41 mg cm^{-3}), and high compressibility (90%) combined with elastic resilience and instant shape recovery. The challenges are overcome facing ultra-lightweight aerogels, including poor mechanical integrity and the inability to form predefined 3D constructs with on-demand functionality, for a multitude of applications. The controllable nature of the coined methodology enables tunable electromagnetic interference shielding with high specific shielding effectiveness (39 893 dB cm^2 g^{-1}), and one of the highest-ever reported oil-absorption capacities (487 times the initial weight of aerogel for chloroform), to be obtained. These properties originate from the engineerable nature of liquid templating, pushing the boundaries of lightweight materials to systematic function design and applications.

1. Introduction

The use of interactions at the interface between two immiscible liquids is an emergent strategy to assemble nanoparticles (NPs) in a constrained setting, spurring much academic interest, since it underpins many technological developments.[1] The soft liquid–liquid interface provides an ideal platform to assemble chemically tailored NPs into densely packed 2D arrays on planar and curved interfaces, which can be easily integrated into 3D meso- and macroscale constructs.[2] Such a controllable approach allows the generation of hierarchical soft materials, where the inherent characteristics of NPs are integrated into the final assembly to impart unique electrical, magnetic, optical, and stimuli-responsive properties.[1a,2a]

The interfacial interactions between functionalized NPs dispersed in one liquid and oligomeric/polymeric ligands with complementary functionality dissolved in a second immiscible liquid form so-called nanoparticles surfactants (NPSs) at the interface, markedly increasing the binding energy of the NPs to the interface.[3] This

S. A. Hashemi, A. Ghaffarkhah, M. Goodarzi, M. Arjmand
Nanomaterials and Polymer Nanocomposites Laboratory
School of Engineering
University of British Columbia
Kelowna, BC V1V 1V7, Canada
E-mail: mohammad.arjmand@ubc.ca

A. Nazemi, A. S. Milani
Composites Research Network-Okanagan Laboratory
School of Engineering
University of British Columbia Okanagan Campus
Kelowna, BC V1V 1V7, Canada

The ORCID identification number(s) for the author(s) of this article can be found under https://doi.org/10.1002/adma.202302826

DOI: 10.1002/adma.202302826

G. Banvillet, O. J. Rojas
Bioproducts Institute
Department of Chemical & Biological Engineering
Department of Chemistry and Department of Wood Science
2360 East Mall
The University of British Columbia
Vancouver, BC V6T 1Z3, Canada

M. Soroush
Department of Chemical and Biological Engineering
Drexel University
Philadelphia, PA 19104, USA

S. Ramakrishna
Department of Mechanical Engineering
Center for Nanofibers and Nanotechnology
National University of Singapore
21 Lower Kent Ridge Road, Singapore 119077, Singapore
E-mail: seeram@nus.edu.sg

process leads to the formation of robust NPS assemblies at the liquid–liquid interface between two immiscible liquids, eventually leading to a jamming of the interfacial assemblies. These jammed assemblies can support compressive loads, enabling the structuring of liquids. Interfacially jammed assemblies can be used to stabilize a jetted stream of one liquid into a second immiscible liquid, i.e., all-liquid 3D printing, by locking the liquids into non-equilibrium shapes.[3c,4] The jamming of NPs at the interface, key to structuring the liquid constructs, results from the formation of a percolated pathway of NPSs capable of withstanding compressive loads imposed on the assembly.[5] This cooperative assembly can be used to form multifunctional building blocks, allowing the development of the next generation of stimuli-responsive soft matter with applications ranging from all-liquid electronics to bicontinuous separation systems and biphasic reactors.[1c,5a,6]

The key to liquid structuring is to overcome the applied pressure gradients on the liquid jet and resulting instabilities. According to the Plateau–Rayleigh instabilities, upon the injection of a falling liquid jet into another medium, beyond a given distance, the liquid jet will be accelerated and lengthened, leading to a decline in the jet's radius, increasing the surface area of the jet relative to the volume. The instability leads to characteristic periodic oscillation in the jet diameter. The increase in the amplitude of these oscillations increases the curvature sites on the falling jet, viz., causing concave and convex sites, giving rise to the pressure gradient and thus generating a flux momentum from high-pressure areas (concave areas) to low-pressure areas (convex areas). This induced flux from high- to low-pressure sites decreases the surface area, leading to an increase in Young–Laplace pressure gradients and interfacial tension, resulting in droplet formation to minimize the interfacial area of a droplet of a given volume.[7]

The jammed jets of one liquid in another yield tubular or filamentous liquid constructs by injecting a stream of the liquid containing engineered NPs into the immiscible liquid phase containing active ligands.[2a,8] The efficient generation of filamentous liquid constructs requires the formation, assembly, and jamming of NPSs that are more rapid than the flow of liquids to change shape to minimize the interfacial area. The solid-like layer of jammed NPSs encasing the tubular liquid thread preserves the integrity of the liquid construct.[1a,5a,9] The filamentous liquid construct can be transformed into a 3D aerogel by removing the liquids via evaporation or lyophilization, where the resulting aerogel is self-supporting and porous on multiple length scales.[8,10] A multi-length-scale porosity is advantageous for designing reconfigurable and engineerable aerogels for advanced applications, such as electromagnetic interference (EMI) shielding and human motion monitoring.[8]

There is still, though, a huge gap in the generation of robust filamentous liquid constructs with tailored compositions, since the required rapid interfacial assembly to reduce interfacial tension and suppress the Plateau–Rayleigh instabilities limits its materials selection to achieve the desired responsiveness to selected stimuli.[8,10] Here, we addressed this by developing a process, termed "liquid templating," where hydrophilic NPs, e.g., graphene oxide (GO), GO decorated with Fe_3O_4 (GO-Fe_3O_4), and cellulose nanofibers (CNFs), very rapidly assemble at the interfaces of two immiscible liquids, enabling the formation of filamentous liquid threads with an on-demand composition. This process allows the assembly of tailored NPs at the liquid–liquid interface and the stabilization of filamentous structures that constitute a template for producing stimuli-responsive 3D filamentous aerogels, enabling the engineering from the nanoscale chemistry to assemblies on the micro- and macroscale. The hierarchical 3D multi-scale arrangement and robust interfacial skin of these aerogels allow the production of ultraflexible soft constructs capable of withstanding 90% compressive strain combined with a very rapid shape recovery. By tuning the functionality, porosity level, and composition of the aerogels, exceptional and controllable EM shielding characteristics are observed, while the superoleophilic character of the aerogels affords record-high oil-absorption capacities, enabling effective oil/water separation or recovery through structural and compositional engineering of aerogels.

2. Results and Discussion

Figure 1 shows the different stages of liquid templating: i) formation of the liquid template upon electrostatic interaction between ligand and NPs (Phase I); ii) freezing of the liquid template (Phase II); and iii) lyophilization of the liquid template to form an aerogel with a porous core surrounded by a solid skin (Phase III). Upon pressure-adjusted jetting of the aqueous phase containing NPs into hexane containing PSS-[3-(2-aminoethyl)amino]propylheptaisobutyl substituted (POSS-NH_2), initially, the POSS-NH_2 rapidly assembles at the interface, forming a positively-charged POSS-NH_3^+ layer that reduces the interfacial energy and suppresses Plateau–Rayleigh instabilities. Subsequently, the GO flakes diffuse to and assemble at the interface, and then the

S. Wuttke
Basque Centre for Materials
Applications & Nanostructures (BCMaterials)
Bld. Martina Casiano
3rd. Floor UPV/EHU Science Park Barrio Sarriena s/n, Leioa 48940, Spain
S. Wuttke
IKERBASQUE
Basque Foundation for Science
Bilbao 48013, Spain
T. P. Russell
Polymer Science and Engineering Department
University of Massachusetts Amherst
120 Governors Drive, Amherst, MA 01003, USA
E-mail: russell@mail.pse.umass.edu
T. P. Russell
Materials Sciences Division
Lawrence Berkeley National Laboratory
1 Cyclotron Road, Berkeley, CA 94720, USA
T. P. Russell
Advanced Institute for Materials Research (WPI-AIMR)
Tohoku University
2-1-1 Katahira, Aoba, Sendai 980–8577, Japan
M. Kamkar
Multi-scale Materials Design Center
Department of Chemical Engineering
Waterloo Institute for Nanotechnology
University of Waterloo
200 University Avenue West, Waterloo, Ontario N2L 3G1, Canada
E-mail: milad.kamkar@uwaterloo.ca

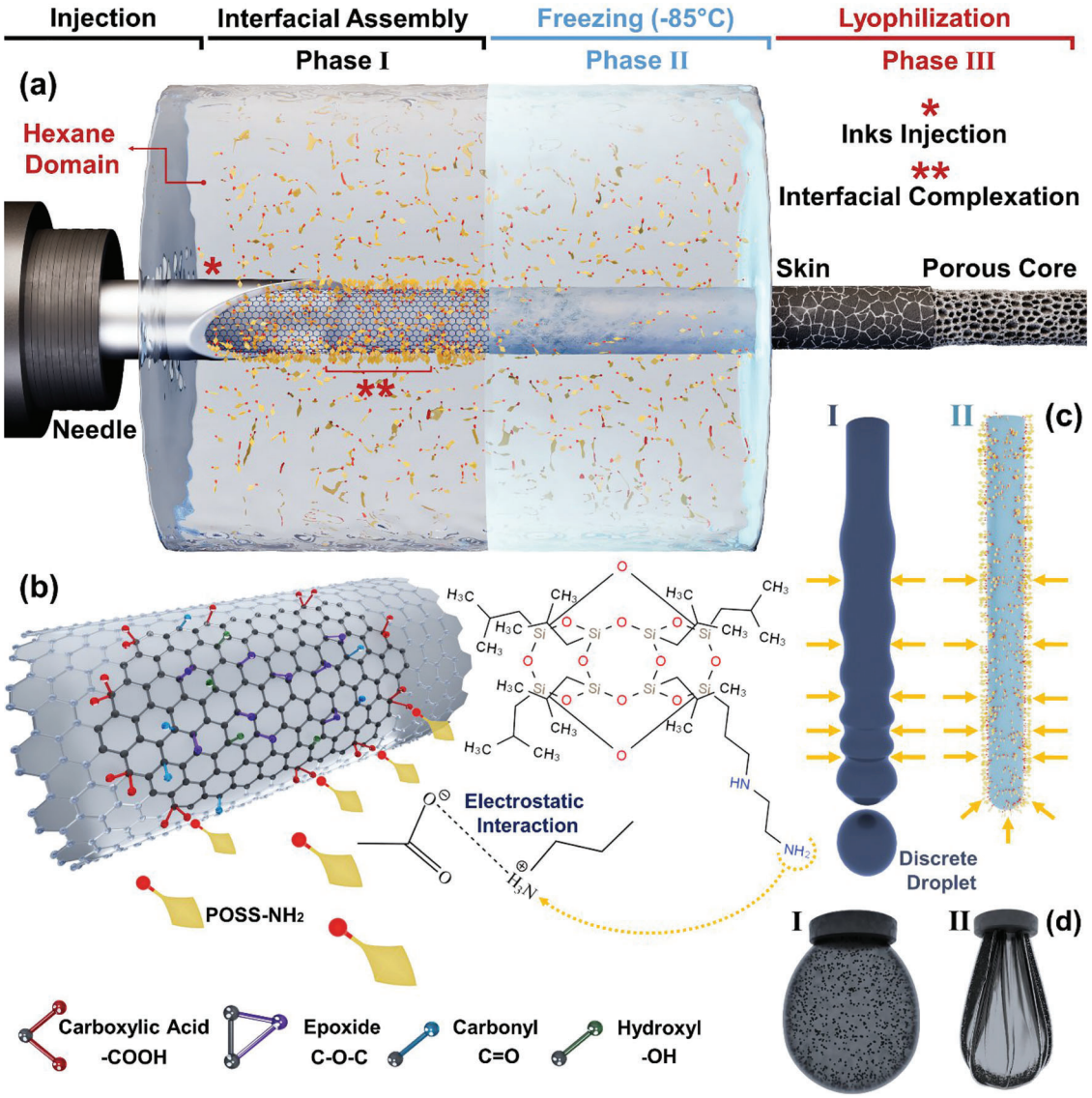

Figure 1. Schematic illustration of the liquid templating methodology. a) The coined process for generating hierarchical 3D aerogels with desired components and functionality, starting from injecting aqueous phase containing GO into an immiscible liquid, i.e., hexane, containing POSS-NH_2 (Phase I) to freezing of liquid template (Phase II) and subsequent lyophilization to generate filamentous aerogels (Phase III). The aerogels comprise core–shell filaments with a thin solid skin wrapped around a porous core. In Phase I, * showcases the injection of aqueous GO-based inks into the hexane domain containing POSS-NH_2, and ** indicates the interfacial complexation, viz., electrostatic interaction of ligands and NPs. As illustrated in Phase II, the placement of the aqueous liquid template into a freezer at −85 °C leads to its freezing, whereas the hexane domain remains liquid owing to its low freezing point (−95.3 °C), enabling its separation before lyophilization. b) Electrostatic interaction of POSS-NH_2 molecule with GO through carboxylic acid deprotonation and amine functional group protonation. c) I) Break up of the liquid stream into discrete droplets to suppress instabilities, and II) enhanced integrity of the liquid stream upon formation of NPSs at the interface, locking in the non-equilibrium shape of the liquid construct in the form of the filament. d) The shape of the droplet in pendant drop tensiometry, I) in equilibrium without the presence of POSS in the oil phase and II) in non-equilibrium shape upon the formation of a solid skin around the droplet as a result NPSs jamming, holding the integrity of liquid construct; the black dots in the image represent the GO dispersed in the aqueous phase.

deprotonated carboxylic acid (–COO^-) groups of GO electrostatically interact with the protonated amine groups (–NH_3^+) of POSS-NH_3^+.[2a] This electrostatic interaction between the ligand and NPs forms an assembly of nanoparticle surfactants (NPSs). The driving force of this pH-dependant electrostatic interaction stems from the pKa value of amine (≈9) and carboxylic acid (≈4.2) functional groups, allowing their protonation and deprotonation when the pKa value becomes higher and lower than the pH of the medium, respectively. This produces robust electrostatic interactions, leading to a cooperative interfacial complexation between the ligand and NPs, generating disordered assemblies at the interface, further reducing the interfacial energy, and leading to a skin around the filament.[1a,2a,11] The selection of POSS-NH_2 as a ligand for this process is advantageous because of its high interfacial activity and rapid diffusion to the interface, enabling the formation of NPSs. This process forms a robust interfacial skin at

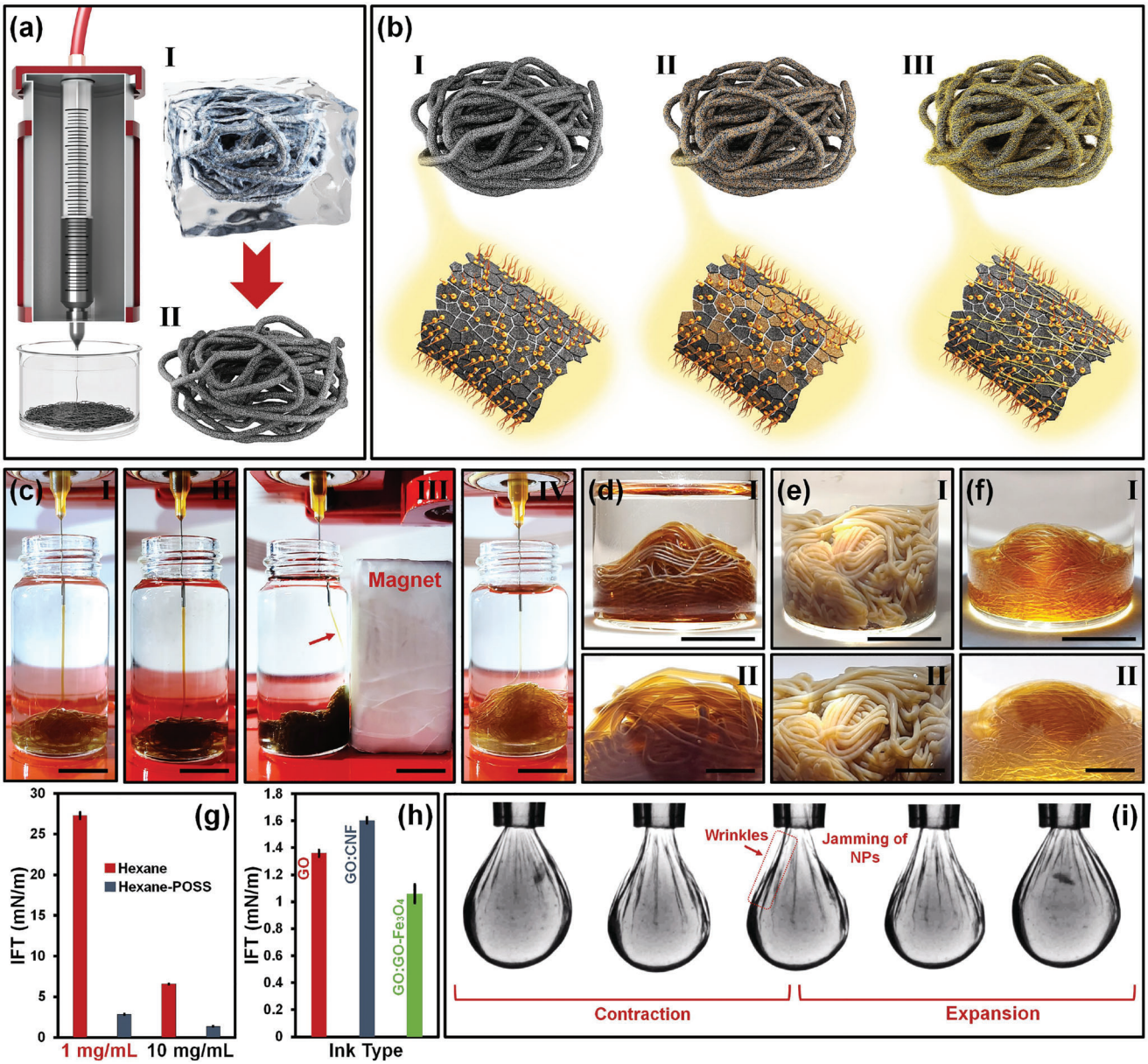

Figure 2. a) Schematic illustration of 3D aerogels formation, showcasing: I) the freezing of the liquid template and II) the formation of aerogel after lyophilization. b) Production of aerogels with different compositions and characteristics, including: I) GO aerogel, II) GO-Fe aerogel, and III) GO-CNF aerogel; in this image, the brownish flakes in (II) represent the GO-Fe_3O_4 flakes and the fibers on the aerogel in (III) denote CNFs. c) Microfluidic injection of different aqueous inks, including: I) GO ink, II,III) GO:GO-Fe_3O_4 ink, and IV) GO:CNF ink into the non-polar hexane domain containing 1 mg mL^{-1} POSS-NH_2; the concentrations of all inks were set at 10 mg mL^{-1}. d–f) Formation of 3D liquid constructs out of GO ink (d), GO:GO-Fe_3O_4 ink (e), and GO:CNF ink (f). Scale bars are equal to (I) ≈14.1 mm, (II) ≈13.9 mm, (III) ≈14.7 mm, and (IV) ≈13.9 mm in (c), (I) ≈12.3 mm and (II) ≈3.8 mm in (d), (I) ≈12.9 and (II) ≈6.8 mm in (e), (I) ≈12.2 mm and (II) ≈6.1 mm in (f). Of note, the showcased images in parts (c–f) were taken using a digital camera, and their scale bars are approximate. g) Interfacial characteristics of different concentrations of aqueous GO suspension in non-polar hexane domains with and without POSS-NH_2 (1 mg mL^{-1}). h) Interfacial tension of different aqueous inks containing GO, GO:CNF, and GO:GO-Fe_3O_4, with an initial concentration of 10 mg mL^{-1} in the hexane domain containing 1 mg mL^{-1} POSS-NH_2. i) Contraction and expansion assays of 1 mg mL^{-1} aqueous GO suspension within the hexane-POSS-NH_2 medium; the wrinkles formed on the droplets imply the formation of elastic assemblies at the interface, i.e., interfacial complexation, as a result of NPs jamming.

the interface of two immiscible liquids, preserving the integrity of filamentous liquid templates.[2c,8] Freezing and lyophilizing the liquid templates lead to the formation of engineerable filamentous aerogels consisting of core–shell filaments composed of a robust solid skin wrapped around a porous tubular core.

A 3D printer is used for microfluidic injection of aqueous inks containing tailored NPs, i.e., GO (10 mg mL^{-1}), GO:GO-Fe_3O_4 (1:1 (weight ratio), 10 mg mL^{-1}), and GO:CNF (1:1, 10 mg mL^{-1}), (**Figure 2**a) into a POSS-NH_2 solution in hexane. Initially, POSS-NH_2 assembles at the interface between the two immiscible

liquids, reducing the interfacial tension. The engineered NPs dispersed in the aqueous phase then diffuse into the interface and electrostatically bond to the POSS-NH_2, forming NPSs that jam at the interface. This leads to the formation of a solid-like layer around the tubular liquid thread, locking in the non-equilibrium shape of tubular filamentous liquid threads. The attachment rate depends on the NPs concentration and their diffusion coefficient in the aqueous phase.[12] The liquid phase is then rapidly frozen (Figure 2a (I)) and lyophilized to yield 3D filamentous ultra-lightweight aerogels with the characteristics of the assembled NPs (Figure 2a (II)). This methodology allows the generation of on-demand 3D structured aerogels with controllable functionality and porosity (from microscale to macroscale) by tuning the concentration/type of NPs, injection medium, injection parameters, and needle size. Figure 2b shows schematics of the hierarchical 3D filamentous aerogel composed of GO (GO aerogel) (I), GO:GO-Fe_3O_4 (GO-Fe aerogel) (II), and GO:CNF (GO-CNF aerogel) (III), where the shape or 3D architecture, diameter of the tubular filaments, composition and concentration of the substances, conductive and/or magnetic characteristics, and the stimuli responsiveness of these aerogels can be engineered by varying the chemical composition of constituent NPs and the ligands.

As a direct consequence of reducing interfacial area and the associated compressive forces to the tubular liquid construct, generating stable jets of water in oil, e.g., hexane, and reaching the on-demand characteristics in liquid templating require precise nanoscale engineering of the chemistry of the GO, GO-Fe_3O_4, and CNF with predefined features. As evidenced in Section S2 (Supporting Information), the GO flakes have inherent functionalities, i.e., active carboxylic acid functional groups, that undergo electrostatic interactions with the ligands and form a robust skin around the liquid thread, enabling the liquid templating of aqueous inks containing hydrophilic nanoscale engineered GO-Fe_3O_4 and CNF NPs. The strong interfacial activity of GO enables the generation of filamentous liquid templates from GO (Figure 2c (I) & Video S1, Supporting Information), GO:GO-Fe_3O_4 (Figure 2c (II,III) & Video S2, Supporting Information), and GO:CNF (Figure 2c (IV) & Video S3, Supporting Information) inks, leading to the formation of free-standing tailorable liquid templates of GO, GO:GO-Fe_3O_4, and GO:CNF (Figure 2d–f). Notably, the magnetic liquid jets were responsive to an external magnetic field upon incorporating magnetic GO-Fe_3O_4 flakes into the inks (Figure 2c (III) & Video S4, Supporting Information). Different compositions of the interfacially active nanoscale materials can be used to generate custom liquid templates, demonstrating their versatility in varying the properties of the aerogels.

The strong interfacial activity of GO accounts for the integrity of these liquid constructs, resulting from the co-assembly of nanosheets and POSS-NH_2, forming a strong interfacial NPS skin, completely suppressing the break-up of liquid streams into discrete droplets. This was validated by dynamic interfacial tension (IFT) measured by pendant drop tensiometry (Figure 2g and Figure S7, Supporting Information). Upon injection of an aqueous ink containing 1 and 10 mg mL^{-1} GO into the non-polar hexane domain, the IFT rapidly decreased from ≈49 mN m^{-1} (for neat water and hexane) to 27.28 and 6.56 mN m^{-1}, respectively, demonstrating the surfactant nature of GO and the influence of GO concentration on minimizing the interfacial tension.[8,13] This surfactant-like character of GO arises from its dual hydrophilic–hydrophobic nature having a non-polar basal plane and polar functional groups.[8] However, even with this high interfacial activity, liquid-like GO aqueous suspensions are unable to form filaments in the absence of ligands in the non-polar domain, forming matrix-dispersed emulsions.[10] By injecting the GO ink with concentrations of 1 and 10 mg mL^{-1} into the non-polar hexane domain containing 1 mg mL^{-1} POSS-NH_2, the GO rapidly migrated to the interface and tightly bonded to the ligands, thereby forming NPSs, lowering the IFT to 2.83 and 1.35 mN m^{-1}, leading to a robust solid-like tubular NPSs skin wrapping the aqueous thread. This interfacial skin can lock in the non-equilibrium filamentous shape of the jetted liquid by suppressing the Plateau–Rayleigh instabilities, preventing the break-up of the aqueous jet into discrete droplets.[7,8]

Mixtures of GO along with GO-Fe_3O_4 and CNF showed an equilibrium IFT of 1.05 and 1.60 mN m^{-1} (Figure 2h and Figure S8, Supporting Information), respectively, allowing liquid templating of the hybrid inks upon generation of a GO-based robust interfacial skin around the liquid threads. The beauty of the dual nature of GO is its ability to generate a robust interfacial skin and sustain the integrity of the liquid construct even in the presence of highly hydrophilic NPs (i.e., CNF and GO-Fe_3O_4) in the aqueous phase. This feature paves the way for designing on-demand functionalities.

The formation of the NPSs interfacial skin around the aqueous phase is visualized during the contraction/expansion of the pendent droplet in the non-polar hexane/POSS-NH_2 domain (Figure 2i and Figure S9–11, Supporting Information). As shown, a droplet of 1 mg mL^{-1} aqueous GO suspension is suspended within the non-polar hexane medium containing 1 mg mL^{-1} POSS-NH_2. Upon decreasing the volume of the droplet, the interfacial area decreases, and a compressive force is imposed on the assembly at the interface. This causes wrinkling of the assembly, demonstrating the elastic nature of the interfacial skin (Video S5, Supporting Information). The wrinkle formation implies the secure positioning of GO by POSS-NH_2 at the interface, generating a resilient interfacial thin film as a consequence of overlapping complex assemblies of GO-POSS-NH_2 NPSs. This process leads to the formation of well-arranged 3D filamentous liquid constructs that can be used as a template for aerogel generation.

Interestingly, the versatile nature of the process allows liquid templating in various non-polar solvents. Control experiments show the possibility of stable liquid templating in low freezing point solvents, such as pentane and toluene, capable of being transformed into well-defined aerogels upon freezing and lyophilization (Figure S12, Supporting Information).

Freezing and lyophilizing the structured liquid templates containing the engineered NPs led to the generation of well-arranged ultra-lightweight aerogels with a 3D hierarchical architecture, featuring a unique worm-like morphology with multiscale porosity (**Figure 3**). These structures are among the lightest reported structures in the literature, and the very light hairs of a cactus can withstand their weight (Figure 3a). The post-processing of these aerogels through thermal reduction at 800 °C under argon for 1 h (Figure 3b, the black sample) resulted in aerogel constructs with inherent electrical conductivity (Figure 3c) or stimuli-responsive

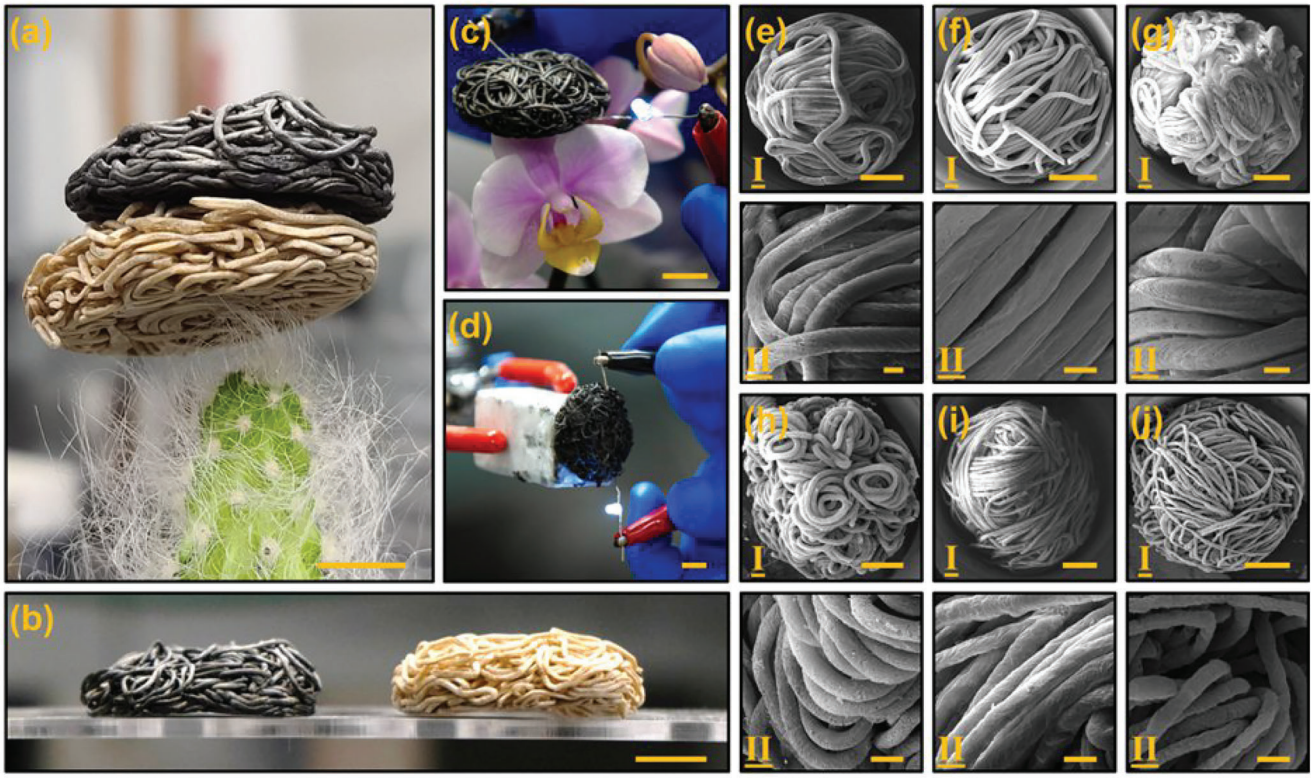

Figure 3. a) Non-reduced and reduced GO aerogels on the very light hairs of cactus. b) A view of the reduced and non-reduced aerogels and a comparison of their size after the thermal annealing at 800 °C under Ar for 1 h. c) A view of lightweight reduced GO aerogel capable of conducting the electricity to light up an LED. d) Combined electrical conductivity and magnetic response in reduced magnetic GO aerogel. e–j) FESEM images of aerogels (I) and zoom in within their filaments (II), including non-reduced GO aerogel (e), reduced GO aerogel (f), non-reduced GO-Fe aerogel (g), reduced GO-Fe aerogel (h), non-reduced GO-CNF aerogel (i), and reduced GO-CNF aerogel (j). Scale bars are equal to: (a) ≈9.5 mm, (b) ≈10.8 mm, (c) ≈11.0 mm, (d) ≈9.7 mm, (e–j) 2 mm (I), and 500 µm (II); the reported values of scale bars in parts (a) to (d) are approximate.

aerogels with a combined magnetic response and high electrical conductivity (Figure 3d). The magnetic aerogels rapidly respond to an external magnetic field while maintaining their integrity (Videos S6 and S7, Supporting Information). Additionally, for shrinkage assessment, a series of raw GO aerogel was prepared using 10 mg mL^{-1} GO ink and injected with a needle gauge of 18 (outer diameter (O.D.) of 1.27 mm). The thermal annealing of the as-prepared GO aerogels at 800 °C in Ar for 1 h leads to an average volume shrinkage rate of 16.60% and a density of ≈3.17 mg cm^{-3} after the reduction process.

Morphological assessment of 3D structured filamentous aerogels prepared with GO, GO:GO-Fe_3O_4, and GO:CNF inks is shown in Figure 3e–j. As seen in the FESEM images, the lyophilization of the frozen templated structured liquids led to the formation of 3D filamentous aerogels with abundant controllable macroscale porosities between filaments. Such a process enables controlling the 3D shape, morphology, size/dimension, and microscale/macroscale porosity of aerogels by adjusting the liquid template for potential applications. FTIR, micro-Raman spectroscopy, and parallel beam X-ray diffraction in Section 4 (Supporting Information) show the formation of a well-established complex between the ligand, i.e., POSS-NH_2, and synthesized NPs.

Tuning the composition of the liquid templates makes it possible to change the arrangement of the microscale pores within the filamentous aerogels after their lyophilization. **Figure 4**a shows a schematic of the different constituents of the core–shell aerogel filaments. These filaments feature tunable internal microscale porosities within filamentous threads from (I) less densely packed hierarchical GO arrangement to (II) hybrid GO:GO-Fe_3O_4 or (III) GO:CNF frameworks with densified porosities. Figure 4b shows the FESEM images of (I) the internal microscale porosities of GO and (II) the formation of a robust solid skin around the porous tubular framework of GO flakes. This interfacially driven robust skin comprised of NPSs is one of the main reasons for the mechanical integrity of the aerogels. The reduced GO aerogel had a high reversible compressibility, capable of reaching compressive strains of 90% and recovering its shape rapidly after force release (Figure 4c and Videos S8 and S9, Supporting Information). Such remarkable mechanical integrity arises from the robust skin around tubular filamentous constructs and the hierarchical GO framework within the core of filaments, enabling compression and shape recovery upon force release. This hierarchical framework results from basal connections of GO flakes, capable of withstanding high compressive strains.[14] Indeed, common ultra-lightweight aerogels suffer from poor mechanical properties, and in most cases, they lose their shape if one touches them. However, the strategy described here generates handleable ultra-lightweight aerogel constructs realizing practical applications.

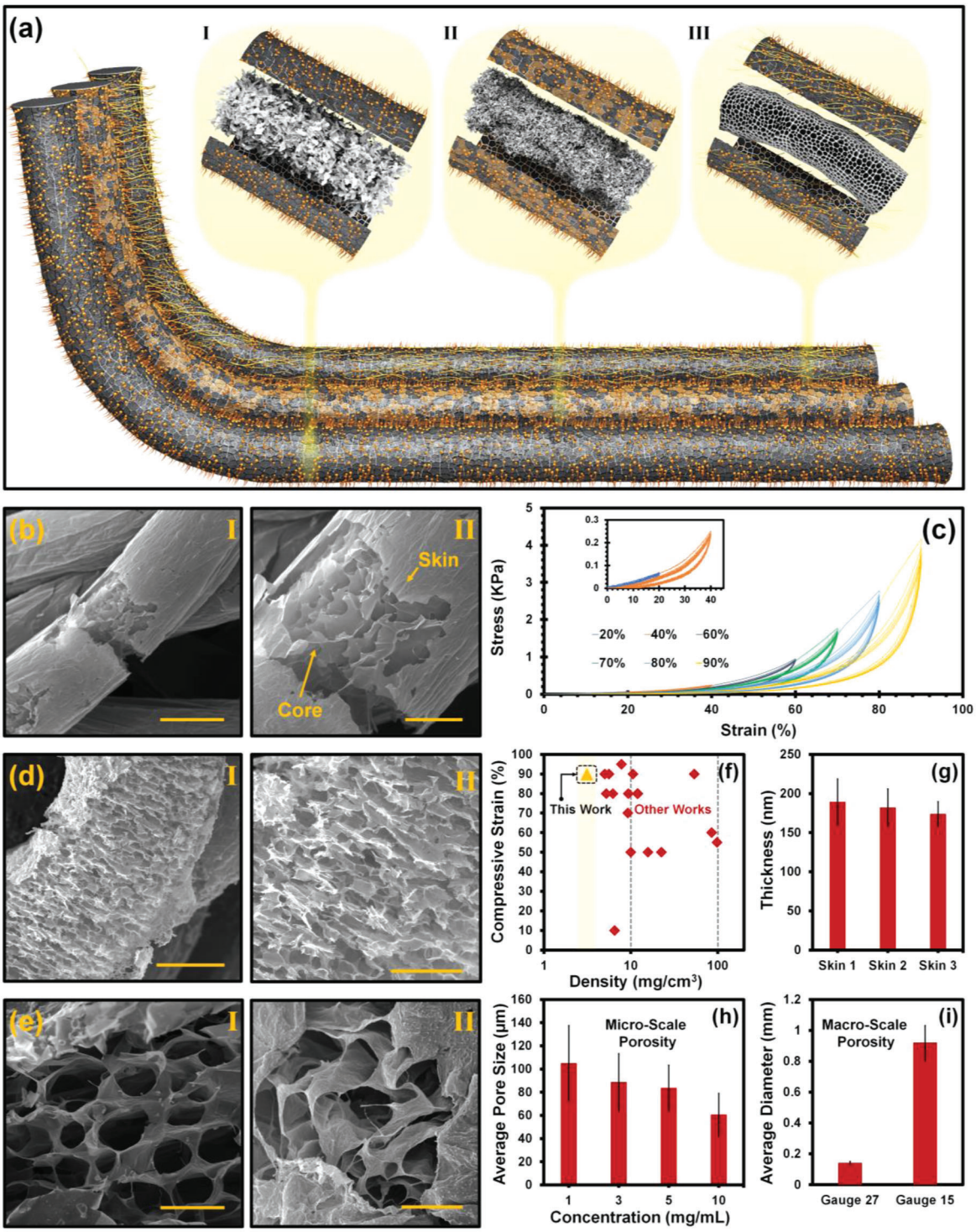

Figure 4. a) Schematic illustration of the tunable internal microscale porosity of aerogel, including GO aerogel (I), GO-Fe aerogel (II), and GO-CNF aerogel (III), via engineering the composition of manipulated NPs and subsequent treatment of the liquid template. b,c) FESEM images of tubular skin and internal microscale porosities of reduced GO aerogel (I,II) (b) and the strain–stress curves of reduced GO aerogel at different compressive strains with six compression cycles at each respective strain rate (c); the inset shows the stress–strain curve of aerogels at 20% and 40% compressive strains. d,e) FESEM images of interfacially driven skin and microscale porosities of reduced GO-Fe aerogel (I,II) (d) and reduced GO-CNF aerogel (I,II) (e). Scale bars are equal to: (b) 500 μm (I) and 200 μm (II), (d) 200 μm (I) and 100 μm (II), and (e) 50 μm (I,II). f) Mechanical performance of the reduced GO aerogel compared with previous examples in the field. g) The average thickness of aerogel skin in different samples. h) Tuning the microscale pore size level of aerogels by changing the concentration of GO from 1 to 10 mg mL^{-1}, and i) manipulating the diameter of the filaments after lyophilization by changing the gauge number of the needle during ink injection or liquid templating.

As evidenced in the FESEM images (Figure 4b (I-II)), lyophilization of the frozen filamentous liquid construct of GO, followed by thermal annealing, led to the formation of an aligned framework of internal microscale porosities. Upon incorporating GO-Fe_3O_4 nanomaterials into GO inks, a more densely packed microscale porous morphology is achieved (Figure 4 d I-II). Introducing naturally harnessed compounds such as CNF along with GO to the hierarchical construct and their simultaneous reduction/carbonization led to the formation of 3D densely packed interconnected microscale porosity arrangements aligned in the direction of the filaments (Figure 4e I,II). The solid skin around the liquid threads and porous graphene framework were also examined by EDX analysis (Section 4.1, Supporting Information). Reducing aerogels by hydrazine vapor treatment or thermal annealing increases the carbon-to-oxygen ratio by removing the oxygen-based functional groups from the aerogel framework, forming a conductive domain of the carbonaceous framework (Figures S16–S27, Supporting Information).

Compared with the previous practices in the field, the aerogels described here show one of the highest elastic resilience at a very low density of 3.12 mg cm^{-3} (Figure 4f and Table S2, Supporting Information), highlighting the remarkable potential of tunable aerogels in advanced applications due to the lightweight of the construct. The thickness of the interfacial solid skin as the main source of integrity and elastic resilience of the aerogels was examined by FESEM after lyophilization of the liquid templates (Figure S28, Supporting Information). Three different GO aerogel samples (10 mg mL^{-1}) were selected, and the thickness of the aerogel filaments' skin was examined at 50 different spots. ImageJ software was used to extract the thickness distribution (Figure S29, Supporting Information). As evidenced in Figure 4g and Figure S28–29 (Supporting Information), average skin thicknesses of 189 ± 29, 182 ± 23, and 173 ± 15 nm were found. The average skin thicknesses for the three aerogel samples were measured to be between 119–242 nm. The formation of NPSs at the interface creates a non-uniform skin around the liquid thread due to the random packing/stacking of NPSs, which is in agreement with previous studies.[15] These densely packed NPSs assemblies could be governed by varying the pH of the medium (promotes the protonation and deprotonation of functional groups), the concentration of ligands and NPs, the ionic strength of the aqueous phase, and the size of NPs.[2a]

The controllable nature of the described process enables fine-tuning the aerogels' microscale and macroscale porosity levels by simply adjusting the processing conditions or manipulating the solid content in the inks. As evidenced in Figure 4h and Figure S30 (Supporting Information), changing the concentration of GO from 1 mg mL^{-1} to 10 mg mL^{-1} led to a change in the average size of microscale porosities and their overall distribution range. As shown in Figure S31 (Supporting Information), the aerogels generated from 1, 3, 5, and 10 mg mL^{-1} aqueous GO suspension exhibited average microscale porosity sizes of 105 ± 32, 88 ± 24, 83 ± 19, and 60 ± 18 μm, respectively. Similarly, changing the gauge number of the injection needle from 27 (O.D. of 0.42 mm) to 15 (O.D. of 1.65 mm) considerably changed the macroscale porosity level. As shown in Figure S32a (Supporting Information), by changing the gauge number of the injection needle from 15 to 27, the volume of the aerogel increased by 32%, leading to a considerable macroscale porosity enhancement. This is also accompanied by a variation of the aerogel filaments diameter, as reducing the needle size during the injection from gauge 15 to 27 could change the average diameter of filaments from 0.92±0.11 to 0.14±0.01 mm (Figure 4i and Figure S32b–e, Supporting Information) after lyophilization. These results highlight the potential of the liquid templating approach in controlling the multilevel porosity of aerogels based on demand.

All in all, the interfacially driven morphologies lock in the characteristics of engineered NPs into the final liquid construct, resulting in a liquid template for developing engineerable/reconfigurable ultra-lightweight aerogels with well-defined nano-, micro-, and macroscale characteristics. Such a function-led design control over structure and composition offers many advantages for engineering desired functionalities within the aerogel framework for electromagnetic protection and environment-related applications.

As a proof of concept, 3D fibrous electromagnetic interference (EMI) shields with tunable shielding characteristics were fabricated. These shields can mitigate the adverse effects of EM waves on the health of living creatures and safeguard the proper performance of electronic equipment.[16] As an essential requirement for EMI shielding, the electrical conductivity of GO, GO-Fe, and GO-CNF aerogels was enhanced by thermal annealing, reaching a conductivity of 0.117, 0.110, and 0.356 S cm^{-1} (**Figure 5**a), respectively, at a thickness of 4 mm for the developed frameworks. Notably, the aerogel frameworks were ultralightweight with densities between 3.05–3.41 mg cm^{-3} after the reduction process (Figure 5b), rendering them practical for applications where weight is a major concern, such as aerospace. Of note, the density of aerogels was measured by calculating the volume and weight of five different aerogel samples and considering the average value. This low weight can promote the reduced aerogels' electrostatic response (Video S10, Supporting Information). The unique multiscale porosity, high electrical conductivity, and the customizability of nanoscale building blocks render these aerogels an engineerable 3D filamentous framework for generating EMI shielding with an on-demand dominant shielding mechanism.

An overview of the shielding characteristics of these aerogels is given in Figure 5c,d and Figure S33 (Supporting Information). The thermally reduced GO aerogel had a reflection dominant (R: 0.54 and SE_R: 3.41 dB) shielding characteristic with excellent absorption loss (SE_A) of 36.23 dB, total shielding effectiveness (SE_T) of 39.64 dB, and specific shielding effectiveness (SSE/t) of 31 739 dB cm^2 g^{-1}. These shielding characteristics arise from different phenomena. A portion of the EM wave incident on the surface of a conductive shield is reflected, owing to the impedance mismatch between free space (377 Ω) and the shield's surface.[16] Reflection is the dominant shielding mechanism for highly conductive EM shields such as metals because of the enforced oscillation of free charge carriers in response to incident EM waves, generating a scattered field as reflection. The portion of the EM waves that penetrates the aerogels faces numerous interfaces with impedance mismatches due to the multiscale (from microscale (in the core of filaments) to macroscale (between filaments)) porosities. These porosities contribute to the multiple internal reflections of the EM waves within the aerogel framework, prolonging their propagation pathway prior to transmission and thus dissipating EM waves in the form of heat. This leads to ab-

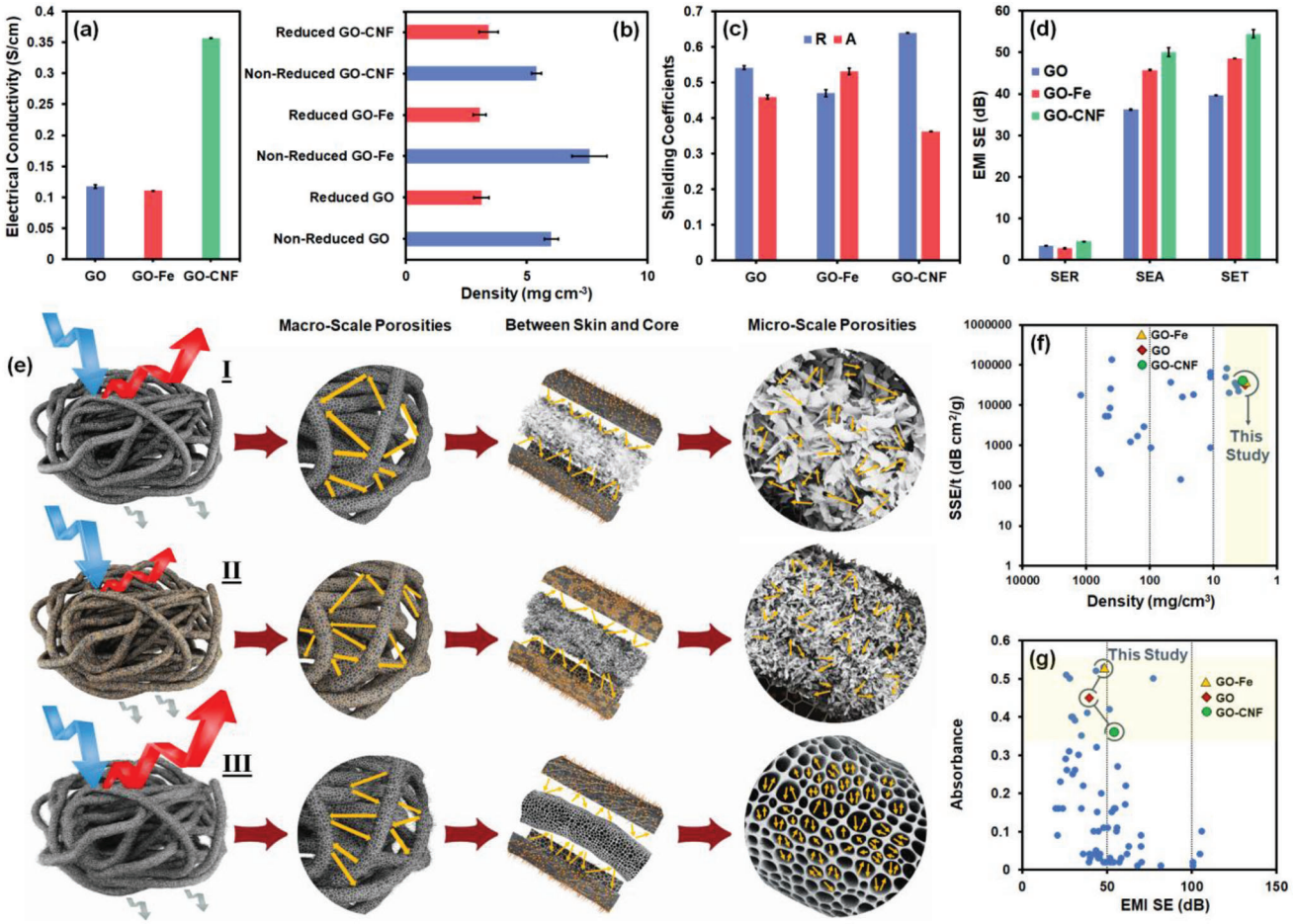

Figure 5. a) Electrical conductivity of the aerogels after thermal annealing at 800 °C for 1 h under Ar. b) Density of aerogels before and after thermal reduction. c) Shielding coefficient, and d) EMI shielding performance of the reduced aerogels within the X-band frequency range (8.2–12.4 GHz). e) Schematic illustration of shielding behavior of multiscale aerogel shields made of reduced GO aerogel (I), reduced GO-Fe aerogel (II), and reduced GO-CNF aerogel (III). f) Density-dependant shielding effectiveness of thermally annealed (800 °C for 1 h under Ar) engineerable aerogels compared with recent practices in the field, and g) comparison of the total shielding and absorbance of the thermally reduced engineerable aerogels compared with recently developed shields; the reported values showcase the controllable shielding characteristics of the generated aerogels.

sorption because of the interaction of EM waves with electrically conductive components and/or electric/magnetic dipoles.[16] Full details of the EMI shielding mechanisms are delineated in Supporting Information.

Considering the governing factors in EMI shielding, it is possible to further enhance the shielding performance of the aerogels by tuning their nanoscale composition and micro-/macroscale porosity by engineering the templated liquids. Here, the introduction of GO-Fe_3O_4 to the aerogel framework boosted the SE_A and SE_T to 45.72 dB and 48.49 dB, respectively, with a dominant absorption mechanism (R: 0.46 and SE_R: 2.76 dB) and remarkable SSE/t of 39 692 dB cm^2 g^{-1}. This considerable increase in the shielding and change in the nature of the shield from a reflector to an absorber at the same ink concentration (1 wt%) arises from an increase in the internal microscale and macroscale porosities, as evidenced by the FESEM images (Figure 4). This increase in the porosity level promotes internal scattering between alternating magnetic/conductive domains, contributing to the dissipation rate of EM waves. More importantly, the introduction of nanoscale magnetic components enhances frequency-dependent magnetic losses. Thus, within the X-band frequency range (8.2–12.4 GHz), EM wave dissipative factors such as eddy current loss and natural resonances are activated, further improving EM shielding performance.[17]

The carbonization of natural compounds, like CNF, within the aerogel framework, along with the GO reduction, leads to a further increase in the level of microscale porosity and electrical conductivity (Figure 4 and Figure 5a). For example, the carbonized/reduced GO-CNF aerogel showed a remarkable SE_A of 50.01 dB, SE_T of 54.47 dB, and SSE/t of 39 893 dB cm^2 g^{-1} with a reflection dominant characteristic (R: 0.63 and SE_R: 4.45 dB) because of the enhanced electrical conductivity, promoting the impedance mismatching.

These results dramatically show that the controllable shielding behavior of the aerogels is due to the multiscale tunability of the templated liquid, i.e., tunable nanoscale building blocks and micro-/macroscale porosities. Figure 5e shows a schematic of the shielding mechanism of the aerogels by engineering their structure via macroscale manufacturing, microscale assembly, and nanoscale chemistry. The EM characteristic of the aerogels

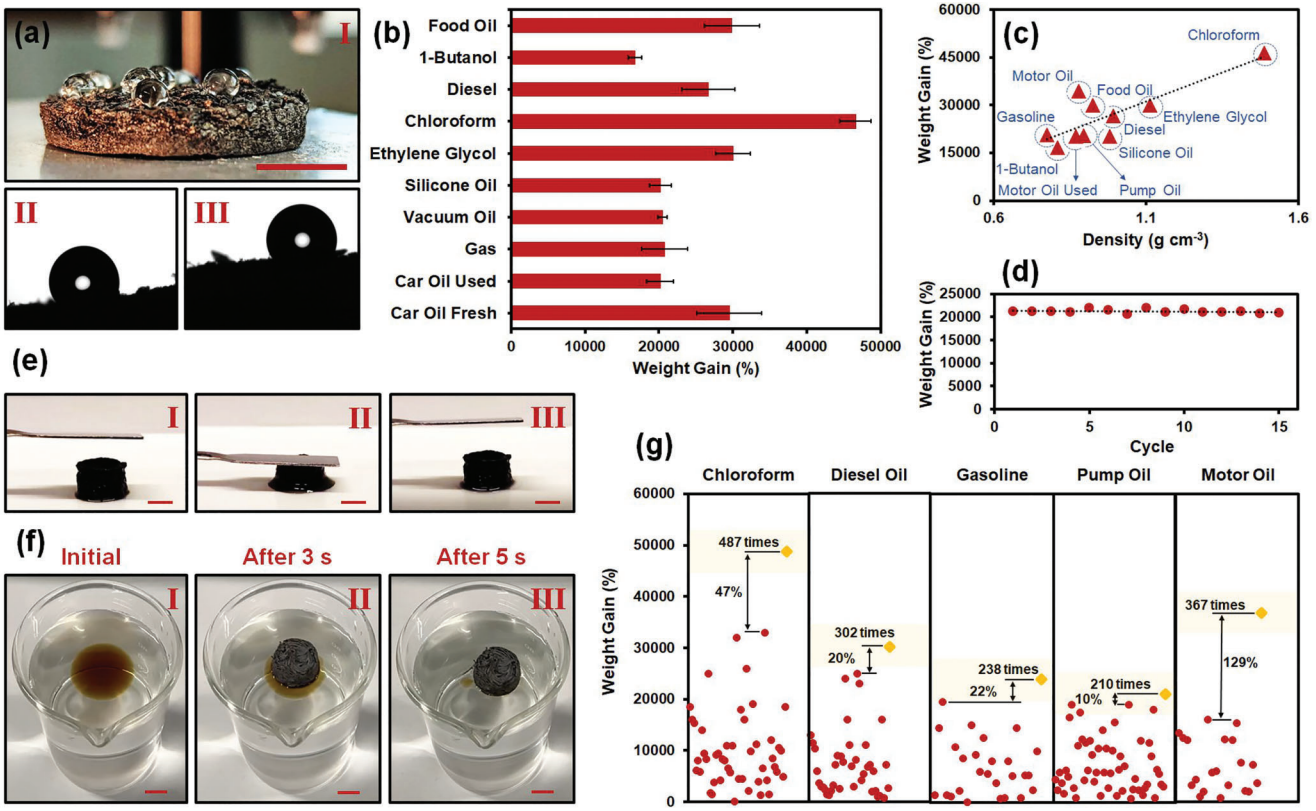

Figure 6. a) Digital images of hydrophobic double-reduced GO aerogel (I) and its hydrophobicity assessment via sessile drop technique (II,III). b) Oil-absorption performance of the double-reduced GO aerogels. c) Oil-absorption capacity over the density of absorbed oils. d) Oil absorption–desorption stability of the double-reduced GO aerogel. e) Prompt oil absorption–desorption cycle of double-reduced GO aerogel upon squeezing. f) Rapid absorption and separation of the used motor oil from the aqueous system via the double-reduced GO aerogel. g) Oil-absorption record of the as-developed aerogels compared with existing records. In the image, the overall amount of weight gain after oil absorption compared with the initial weight of the aerogel and the oil-absorption enhancement is compared with the best practices in the field; the *X*-axis denotes the data point number with no specific order. Scale bars are equal to: a) ≈10.7 mm (I), e) ≈9.4 mm (I), ≈9.8 mm (II) and ≈10.1 mm (III), and f) ≈9.2 mm (I), ≈9.1 mm (II), and ≈9.1 mm (III). The reported scale bars in (a), (e), and (f) are approximate.

developed here is compared with other aerogels reported previously in terms of their specific shielding effectiveness (Figure 5f and Table S3, Supporting Information) and absorbance (Figure 5g and Table S4, Supporting Information) at a low ink concentration (1 wt%).

One of the most formidable global threats stems from the leakage of crude or heavy oil, as well as highly toxic organic solvents, into the environment. These leaks endanger marine life, contaminate seafood, pollute freshwater sources, and introduce a considerable volume of toxic compounds into the ecosystem. This issue gives rise to substantial ecological, economic, and health concerns in affected areas. As such, it necessitates the development of effective solutions capable of overcoming the common drawbacks of conventional methods. These disadvantages include the release of toxic dioxins due to oil combustion, subpar solvent or oil absorption efficiency, prohibitive production costs, inadequate recyclability, and compromised structural integrity.[18] We addressed this global challenge using mechanically robust, multiscale porous hierarchical aerogel constructs capable of effectively recovering a large amount of toxic oils or solvents without causing secondary pollution.

To demonstrate the practicality of the aerogel constructs for global oil/solvent contamination, a wide range of highly contaminating and widely used solvents/oils were selected, from low-density and highly volatile ones to heavier oils/solvents. For this purpose, the tubular solid-like layer around the filamentous threads generated from the NPS derivatives, i.e., siloxane groups of POSS-NH_2 and reduced GO flakes, makes the aerogel construct hydrophobic (contact angle of 120.5°) with a remarkable superoleophilicity (**Figure 6**a (I-III)). Due to the abundant microscale porosities within the filamentous aerogels and the macroscale porosities between the filaments, the aerogels offered an exceptional oil-absorption capacity (Figure 6b). The double-reduced GO aerogel had one of the highest oil-absorption capacities ever achieved by absorbing chloroform, diesel oil, motor oil, and pump oil more than 466 ± 21, 345 ± 22, 204 ± 6, and 266 ± 35 times of its original weight, respectively, which was found to be nearly density-dependent (Figure 6c). Notably, the double-reduced GO aerogels were generated upon an initial reduction via hydrazine vapor at 100 °C followed by thermal annealing at 800 °C for 1 h under Ar (see Supporting Information for more details).

Outstanding properties of these aerogels, including mechanical robustness and an extremely flexible structure, enable repeated absorption–desorption cycles without considerable changes in their absorption capacity (Figure 6d). We note that the ease of processing and scalability of the process renders it a versatile approach to meeting industrial demands at large scales. The aerogel, saturated with the oils, maintained its mechanical integrity and flexibility, and released the absorbed oil simply by squeezing (Figure 6e); Video S11 (Supporting Information) shows the instant absorption–desorption of diesel oil by the double-reduced 3D structured filamentous GO aerogel. Upon oil desorption by compression, the aerogel promptly recovers its initial shape without any visible plastic deformation, attesting to its elastic resilience and superior compressive resistance (Figure 6e). The aerogel could also simply float on the surface of the water, rapidly separating the oil from the water in less than 5 s (Figure 6f and Video S12, Supporting Information), rendering these aerogels appealing for oil spill remediation. The fact that these novel porous ultra-lightweight solids feature exceptional oil-absorbance properties (Figure 6g and Table S5, Supporting Information) coupled with straightforward processability will empower them to challenge current market solutions. Besides, such recoverability, fast absorption kinetics, prevention of secondary pollution, and controllable structural features make these aerogels a versatile framework for the effective cleanup of nature from hazardous oil/solvent pollution.

3. Conclusions

We have developed a practical methodology for designing filamentous liquid templates, namely "liquid templating," with custom composition and arrangement for task-oriented aerogel production through lyophilization. The methodology enables the integration of NPs into structured liquids for the macroscale manufacturing of filamentous aerogel constructs with controllable characteristics, porosity level (from micro- to macroscale), 3D architectural design, morphology, responsiveness, and functionality. The generated ultra-lightweight aerogels with a density between 3.05–3.41 mg cm^{-3} at a reduced state showed remarkable mechanical integrity, capable of 90% compressibility with very rapid shape recovery, overcoming a critical problem with aerogels, viz., brittleness and poor mechanical stability. As a proof of function, the tunability of aerogels through governing the liquid templates allowed us to develop EMI shields with controllable shielding characteristics and high shielding effectiveness (SSE/t of 31 739 to 39 893 dB cm^2 g^{-1}). The double-reduced GO aerogel showed one of the highest ever-recorded values for oil or organic solvent absorption, with the ability to rapidly absorb 487 times their original weight (for chloroform), showcasing considerable improvement in the oil-absorption capacity compared with the best practices in the field. In short, liquid templating through interfacial complexation is a strategy that can revolutionize the design of materials, offering a promising approach to enhancing performance far beyond what can be achieved today.

Supporting Information

Supporting Information is available from the Wiley Online Library or from the author.

Acknowledgements

S.A.H. and A.G. contributed equally to this research study. This research is financially supported by the Natural Sciences and Engineering Research Council of Canada (NSERC) with funding reference number ALLRP 555586-20. The authors acknowledge the Syilx Okanagan Nation for using their traditional, ancestral, and unceded territory, the land on which the research was conducted. M.A. would like to thank the Canada Research Chairs program (CRC-2018-00234) for the financial support. T.P.R. was supported by the U.S. Department of Energy, Office of Science, Office of Basic Energy Sciences, Materials Sciences and Engineering Division under Contract No. DE-AC02-05-CH11231 within the Adaptive Interfacial Assemblies Towards Structuring Liquids program (KCTR16). M.K. acknowledges the support of the NSERC Discovery Grant, funding reference number RGPIN-2023-03466. O.J.R. also gratefully acknowledges the Canada Excellence Research Chair Program (CERC-2018-00006), and Canada Foundation for Innovation (project number 38623). The authors acknowledge the support of Fipke Laboratory for Trace Element Research (FiLTER) for access to the scanning electron microscope and S. E. Mhatre, under the supervision of Prof. Orlando J. Rojas, in taking the additional dynamic interfacial tension tests.

Note: Figure 4 was reset on October 19, 2023, after initial publication online.

Conflict of Interest

The authors declare no conflict of interest.

Data Availability Statement

The data that support the findings of this study are available in the supplementary material of this article.

Keywords

electromagnetic interference (EMI) shielding, filamentous aerogels, interfacial assembly, nanoparticle assembly, oil absorption

Received: March 27, 2023
Revised: July 14, 2023
Published online: September 4, 2023

[1] a) R. Xu, T. Liu, H. Sun, B. Wang, S. Shi, T. P. Russell, *ACS Appl. Mater. Interfaces* **2020**, *12*, 18116; b) S. Zhu, G. Xie, H. Cui, Q. Li, J. Forth, S. Yuan, J. Tian, Y. Pan, W. Guo, Y. Chai, Y. Zhang, Z. Yang, R. W. H. Yu, Y. Yu, S. Liu, Y. Chao, Y. Shen, S. Zhao, T. P. Russell, H. C. Shum, *ACS Nano* **2022**, *16*, 13761; c) C. Huang, J. Forth, W. Wang, K. Hong, G. S. Smith, B. A. Helms, T. P. Russell, *Nat. Nanotechnol.* **2017**, *12*, 1060.

[2] a) S. Shi, T. P. Russell, *Adv. Mater.* **2018**, *30*, 1800714; b) J. Forth, P. Y. Kim, G. Xie, X. Liu, B. A. Helms, T. P. Russell, *Adv. Mater.* **2019**, *31*, 1806370; c) S. Shi, B. Qian, X. Wu, H. Sun, H. Wang, H. B. Zhang, Z. Z. Yu, T. P. Russell, *Angew. Chem., Int. Ed.* **2019**, *58*, 18171; d) B. L. Tardy, B. D. Mattos, C. G. Otoni, M. Beaumont, J. Majoinen, T. Kämäräinen, O. J. Rojas, *Chem. Rev.* **2021**, *121*, 14088.

[3] a) H. Sun, M. Li, L. Li, T. Liu, Y. Luo, T. P. Russell, S. Shi, *J. Am. Chem. Soc.* **2021**, *143*, 3719; b) H. Sun, L. Li, T. P. Russell, S. Shi, *J. Am. Chem. Soc.* **2020**, *142*, 8591; c) S. Sun, C. Xie, J. Chen, Y. Yang, H. Li, T. P. Russell, S. Shi, *Angew. Chem., Int. Ed.* **2021**, *60*, 26363; d) R. Grande, L. Bai, L. Wang, W. Xiang, O. Ikkala, A. J. Carvalho, O. J. Rojas, *ACS Sustainable Chem. Eng.* **2019**, *8*, 1137.

[4] P. Y. Gu, F. Zhou, G. Xie, P. Y. Kim, Y. Chai, Q. Hu, S. Shi, Q. F. Xu, F. Liu, J. M. Lu, *Angew. Chem., Int. Ed.* **2021**, *60*, 8694.
[5] a) W. Feng, Y. Chai, J. Forth, P. D. Ashby, T. P. Russell, B. A. Helms, *Nat. Commun.* **2019**, *10*, 1095; b) G. Xie, J. Forth, Y. Chai, P. D. Ashby, B. A. Helms, T. P. Russell, *Chem* **2019**, *5*, 2678; c) X. Hua, M. A. Bevan, J. Frechette, *Langmuir* **2018**, *34*, 4830.
[6] a) X. Liu, N. Kent, A. Ceballos, R. Streubel, Y. Jiang, Y. Chai, P. Y. Kim, J. Forth, F. Hellman, S. Shi, D. Wang, B. A. Helms, P. D. Ashby, P. Fischer, T. P. Russell, *Science* **2019**, *365*, 264; b) L. Li, H. Sun, M. Li, Y. Yang, T. P. Russell, S. Shi, *Angew. Chem., Int. Ed.* **2021**, *60*, 17394.
[7] B. E. Rapp, *Microfluidics: Modeling, Mechanics, and Mathematics*, Elsevier, Amsterdam, The Netherlands **2022**.
[8] M. Kamkar, A. Ghaffarkhah, R. Ajdary, Y. Lu, F. Ahmadijokani, S. E. Mhatre, E. Erfanian, U. Sundararaj, M. Arjmand, O. J. Rojas, *Small* **2022**, *18*, 2200220.
[9] X. Liu, S. Shi, Y. Li, J. Forth, D. Wang, T. P. Russell, *Angew. Chem., Int. Ed.* **2017**, *56*, 12594.
[10] M. Kamkar, E. Erfanian, P. Bazazi, A. Ghaffarkhah, F. Sharif, G. Xie, A. Kannan, M. Arjmand, S. H. Hejazi, T. P. Russell, G. G. Fuller, U. Sundararaj, *Adv. Mater. Interfaces* **2022**, *9*, 2101659.
[11] D. Lin, T. Liu, Q. Yuan, H. Yang, H. Ma, S. Shi, D. Wang, T. P. Russell, *ACS Appl. Mater. Interfaces* **2020**, *12*, 55426.
[12] a) Y. Chai, J. Hasnain, K. Bahl, M. Wong, D. Li, P. Geissler, P. Y. Kim, Y. Jiang, P. Gu, S. Li, D. Lei, B. A. Helms, T. P. Russell, P. D. Ashby, *Sci. Adv.* **2020**, *6*, eabb8675; b) Y. Chai, A. Lukito, Y. Jiang, P. D. Ashby, T. P. Russell, *Nano Lett.* **2017**, *17*, 6453.
[13] F. Kim, L. J. Cote, J. Huang, *Adv. Mater.* **2010**, *22*, 1954.
[14] K. Pang, X. Song, Z. Xu, X. Liu, Y. Liu, L. Zhong, Y. Peng, J. Wang, J. Zhou, F. Meng, J. Wang, C. Gao, *Sci. Adv.* **2020**, *6*, eabd4045.
[15] Z. Sun, T. Feng, T. P. Russell, *Langmuir* **2013**, *29*, 13407.
[16] S. A. Hashemi, A. Ghaffarkhah, E. Hosseini, S. Bahrani, P. Najmi, N. Omidifar, S. M. Mousavi, M. Amini, M. Ghaedi, S. Ramakrishna, M. Arjmand, *Matter* **2022**, *5*, 3807.
[17] J. C. Shu, W. Q. Cao, M. S. Cao, *Adv. Funct. Mater.* **2021**, *31*, 2100470.
[18] a) M. Peng, Y. Zhu, H. Li, K. He, G. Zeng, A. Chen, Z. Huang, T. Huang, L. Yuan, G. Chen, *Chem. Eng. J.* **2019**, *373*, 213; b) X. Yue, Z. Li, T. Zhang, D. Yang, F. Qiu, *Chem. Eng. J.* **2019**, *364*, 292.